

# **Intrinsic one-dimensional conducting channels in the Kondo insulator SmB<sub>6</sub>**

Ke-Jun Xu<sup>1,2</sup>, Mark Barber<sup>1</sup>, Eric Yue Ma<sup>1,2</sup>, Jing Xia<sup>3</sup>, Monica Ciomaga Hatnean<sup>4</sup>,  
Geetha Balakrishnan<sup>4</sup>, Jan Zaanen<sup>5</sup> and Zhi-Xun Shen<sup>1, 2, †</sup>

<sup>1</sup> Geballe Laboratory for Advanced Materials, Department of Physics and Applied Physics, Stanford University, Stanford, California 94305, USA

<sup>2</sup> Stanford Institute for Materials and Energy Sciences, SLAC National Accelerator Laboratory, 2575 Sand Hill Road, Menlo Park, California 94025, USA

<sup>3</sup> Department of Physics and Astronomy, University of California, Irvine, California 92697, USA

<sup>4</sup> Department of Physics, University of Warwick, Coventry, CV4 7AL, UK

<sup>5</sup> Instituut-Lorentz for Theoretical Physics, ΔITP, Leiden University, Niels Bohrweg 2, Leiden 2333CA, The Netherlands

†: [zxshen@stanford.edu](mailto:zxshen@stanford.edu)

## Abstract

Since its discovery as a Kondo insulator 50 years ago,  $\text{SmB}_6$  recently received a revival of interest due to detection of unexpected quantum oscillations in the insulating state, discovery of disorder-immune bulk transport, and proposals of correlation-driven topological physics. While recent transport results attribute the anomalous low temperature conduction to two-dimensional surface states, important alternatives, such as conduction channel residing in one-dimensional dislocation lines, have not been adequately explored. Here we study  $\text{SmB}_6$  with scanning microwave impedance microscopy and uncover evidence for conducting one-dimensional states terminating at surface step edges. These states remain conducting up to room temperature, indicating unusual robustness against scattering and an unconventional origin. Our results bring to light a heretofore undetected conduction route in  $\text{SmB}_6$  that contributes to the low temperature transport. The unique scenario of intrinsic one-dimensional conducting channels in a highly insulating correlated bulk offers a one-dimensional platform that may host exotic physics.

## Introduction

Deriving its charge gap from hybridization of localized 4f states and conduction 5d states, the Kondo insulator  $\text{SmB}_6$  hosts a poorly understood correlated bulk<sup>1,2</sup>. Unlike small-gap band insulators, including topological band insulators such as  $\text{Bi}_2\text{Se}_3$ , where the bulk may be highly conductive due to impurity state  $E_F$  pinning<sup>3</sup>,  $\text{SmB}_6$  has a bulk that remains remarkably insulating and immune from disorder despite an activation gap of  $\sim 5\text{-}10$  meV<sup>4</sup>. While a metallic Kondo lattice system at low temperatures can be considered as a renormalized Fermi liquid with well-defined heavy quasiparticles<sup>5</sup>, whether a Kondo insulator can be thought of as a renormalized band insulator is still an open question. There is little theoretical understanding, other than generalized adiabatic continuity arguments, of how the low temperature insulating state connects to the high temperature incoherent state. The recent interest<sup>6</sup> in  $\text{SmB}_6$  calls for further investigation of the experimental phenomenology, which may help gain insight into the Kondo insulating state. While the theoretical case for topological protection has been proposed<sup>2</sup>, definitive evidence for topological surface states in  $\text{SmB}_6$  is lacking despite extensive experimental

efforts. Previous thickness-dependent and non-local transport measurements in  $\text{SmB}_6$  suggest the ubiquitous low temperature resistivity plateau is due to two-dimensional surface states<sup>7,8,9,10</sup>. However, they have not considered all possible contributions from alternate conduction channels such as one-dimensional states. Specifically,  $\text{SmB}_6$  is claimed<sup>2</sup> to be a translationally active topological insulator<sup>11</sup> protected by time reversal symmetry, where dissipation-less helical modes should form at dislocations<sup>12,13</sup>. On the other hand, while angle-resolved photoemission spectroscopy (ARPES) measurements have detected two-dimensional surface states in  $\text{SmB}_6$ <sup>14, 15, 16, 17, 18</sup>, their origin and topological nature are still under debate<sup>19</sup>. The lack of concrete connection between the transport results and microscopic understanding of surface states in  $\text{SmB}_6$  warrants a thorough search for alternate conduction channels<sup>4, 20, 21</sup>. Here we use scanning microwave impedance microscopy (MIM)<sup>22</sup> to study  $\text{SmB}_6$  and find extended one-dimensional conducting channels perpendicular to the surface. We also discover surprising robustness of these states at high temperatures, revealing another enigma of unconventional physics in  $\text{SmB}_6$ .

MIM is a near-field scanning probe technique using a low-GHz frequency excitation<sup>23</sup>. Compared to detecting DC current, the capacitive coupling of GHz impedance measurements is sensitive to buried or electrically-floating features, without the need for a complete current path to ground. This makes MIM especially suitable for studying conducting channels in bulk insulators<sup>24</sup>. By staying within a few GHz, the excitation is quasi-electrostatic and probes the ground state. A simplified microwave circuit diagram is shown in Fig. 1d. In operations with an oxide or vacuum tip-sample barrier, the change in conductivity of the sample underneath the tip is detected via a change of the overall impedance from only a small volume that is penetrated by the evanescent field around the tip. However, if ohmic contact with a conducting channel is established at any point in the scan, the channel serves as a conductor for the microwave field and extends it beyond the tip. This probes a large sample volume and significantly changes the balance of the reflected signal, resulting in a large signal. Here, we take advantage of the stability of the  $\text{SmB}_6$  surface and its low work function, which allows easier ohmic contact with the tip, and reveal conducting spots which extend beneath the surface.

## Results

We perform MIM on  $\text{SmB}_6$  crystals grown by the aluminum flux<sup>9</sup> and floating zone methods<sup>25</sup>. A typical MIM image of a cleaved (001) flux-grown  $\text{SmB}_6$  surface is shown in Fig. 1b, taken at the indicated area in the optical image in Fig. 1a. The imaginary (Im) channel shows several lines that are topographic artifacts arising from step edges. This results from the slightly different sample-vacuum composition probed by the evanescent field when the tip is on top of a topographic feature, and is a well-established artifact reported in previous MIM works<sup>22, 26</sup>. On top of these step edges, there are scattered conductive spots with very large signals. The large MIM signals at these spots compared to the topographic artifacts can be seen in representative line cuts in Figs. 1e and 1f. The real (Re) channel (Fig. 1c) shows similar spots, but no topographic artifacts, as this channel is only sensitive to dissipation. For the rest of the article, only the Im channel will be shown as it contains both the topographic and MIM information.

In typical MIM experiments with similar excitation power and amplification, the output signal difference between conducting and insulating states during non-ohmic contact scans is about a few tens to hundred mV, depending on the sharpness of the tip<sup>27,28,29</sup>. Here, the conductive spots have signals that are 1-2 orders of magnitude greater, exceeding the maximum analog-digital converter (ADC) range of 10 V. This rules out the scenario of contact to a localized zero-dimensional state, as the large signals observed here require extended states that transmit the microwave field to a large sample volume. Further evidence for non-conventional MIM signal in these conductive dots is shown in Fig. 1e and its inset. The size of the conductive spots, reaching below 20 nm, are significantly smaller than the size of the tip (~100 nm) and the resolution limit of the evanescent field. This demonstrates that the spots are associated with the tip apex contacting the termination point of one-dimensional channels. The locations of these spots are highly repeatable, even under different scanning conditions and temperatures (see supplementary section S4), suggesting that they are intrinsic conducting states and not random ohmic contacts made to the bulk or surface states.

We solidify the one-dimensional nature of the conducting spots by applying a DC voltage bias to the scanning tip, which causes voltage-induced breakdown when the tip is close

to the conducting channels (Fig. 2f). As the tip bias is varied from 0 V to 2 V (Fig. 2a-d), the breakdown regions near the conduction channels increase in size around the original spots, but elsewhere on the sample no breakdown is observed. The breakdown effect can also be seen clearly in the line cuts in Fig. 2e, where the signal near the break down region quickly saturates the ADC as tip bias is applied. After cycling the tip bias back to 0 V, the MIM images partially recovers to the original state. The differences are likely due to remnant break down channels that connects to the original one-dimensional conducting channels. The localized breakdown behavior here rules out the possibility of tunneling to two-dimensional surface states, ensuring the one-dimensional nature of these observed states. We rule out the possibility of small aluminum inclusions as the origin of these conductive spots by measuring samples grown with the floating zone method (supplementary section S5), where we find similar spots at step edges.

To check the validity of the ohmic-contact-enhanced imaging model, we simulate the tip-sample-channel junction with finite element analysis using the AC/DC module in COMSOL Multiphysics (Fig. 3). If there is a thin insulating barrier or vacuum between the tip and sample (Fig. 3a), the coupling remains capacitive, and only small changes in the reflected signal occur when the tip passes over the metallic channel. On the other hand, when the tip is in contact with the channel (Fig. 3b), the electric field permeates deep within the sample bulk. In this case the effective impedance changes dramatically, thereby producing a large signal. Comparing qualitatively to the experimentally measured MIM signals in non-contact (Fig. 3c) and contact (Fig. 3d) geometries, these simulated behaviors show that the anomalous large signals measured in experiment are consistent with the dichotomous scenarios between ohmic and non-ohmic contact.

At first sight, these channels appear to be strikingly consistent with the helical modes associated with dislocations terminating at the surface of a topological insulator<sup>11,12,13</sup>. However, their temperature dependence, shown in Fig. 4a-b, reveals a surprise: these channels are conductive all the way to at least room temperature. The known Kondo energy scales in SmB<sub>6</sub> are the ~50-100 K single ion screening temperature from the magnetic susceptibility peak<sup>30</sup> and ~30-40 K Kondo coherence onset temperature corresponding to the resistivity upturn (Fig. 4c). Thus, the robustness of these one-

dimensional conducting channels at high temperatures poses a challenge to understanding their electronic origin. On the one hand, normal one-dimensional states are generally more susceptible to scattering and localization effects than bulk states<sup>31</sup>. The relatively low Debye temperature of  $\sim 250$  K in the rare earth borides<sup>32</sup> indicates significant phonon scattering at room temperature. Combined with the incoherent Kondo spin scattering, these effects should strongly affect the conductance of trivial defect states, especially given the remarkable resistance of the bulk gap to defects and impurities<sup>4</sup>. On the other hand, the existence of the one-dimensional conducting states in  $\text{SmB}_6$  at temperatures larger than the gap energy scale is not compatible with conventional topological protection in band insulators, which is typically fragile against thermal fluctuations. However, we note that the high temperature state of the Kondo insulator is strongly correlated and cannot be described by a band picture: At room temperature, the bulk resistivity still exhibits insulating behavior (Fig. 4c), suggesting strong spin scattering from the 4f electrons; high temperature ARPES data in  $\text{SmB}_6$  also shows a persistence of incoherent states up to and above room temperature<sup>33</sup>. Thus, there are no quasiparticles at room temperature and the concept of a single particle gap is ill-defined, leaving the high temperature state of  $\text{SmB}_6$  a poorly understood phase of matter. It is not clear theoretically if topological protection can exist in such a state. We further note that the coherent low temperature state and the highly incoherent high temperature state is continuously connected without any phase transitions, suggesting that these two extremes may smoothly deform into one another.

## Discussion

To understand the microscopic origin of these anomalous one-dimensional conducting channels, an immediate phenomenological question is whether the observed channels are indeed associated with dislocations. This is a credible possibility given their status as ubiquitous line-like topological defects that occur naturally in nearly any solid<sup>34</sup>, and similar one-dimensional conducting states have been observed along dislocations in two-dimensional bilayer graphene<sup>35</sup>. Moreover, dislocations in bulk materials typically terminate at step edges on the surfaces, consistent with the MIM observations here. A strategy to substantiate this association is demonstrated in Ref. 36 using scanning

tunneling microscopy on a conventional Bi-type topological band insulator. In addition, one may look for small angle grain boundaries in twinned crystals; these correspond with arrays of dislocations and the resulting two-dimensional boundary metal is predicted host unique topological properties<sup>37</sup>. Finally, dislocation networks can be manipulated by applying external shear stress. As demonstrated in the case of  $\text{Bi}_{1-x}\text{Sb}_x$ <sup>20,21</sup>, such plastic deformations can be employed to observe contributions of the dislocations to macroscopic transport.

Their microscopic interpretation aside, the observed one-dimensional conducting channels already challenge the previously established consensus that the low temperature transport in  $\text{SmB}_6$  is purely dominated by two-dimensional surface states. Being one-dimensional, the observed states here also do not carry current uniformly across the sample, so the overall resistance is not defined by a bulk three-dimensional geometry factor multiplied by the resistivity. As exemplified in Fig. 1b, the step edges and dislocations may be concentrated in only a certain part of the sample. Thus, the thickness-dependent and non-local transport results<sup>7,8,9,10</sup> can be consistent with both one-dimensional or two-dimensional conduction, or a combination of the two. Furthermore, these metallic states also present a new candidate for explaining the anomalous quantum oscillations in the insulating state<sup>38,39</sup>. Local stress around the dislocation may drive a pressure-induced transition to a heavy-mass Fermi liquid metal<sup>40</sup>. The mean free path of  $\sim 10$  nm estimated from the quantum oscillation Dingle damping factor<sup>41</sup> is approximately consistent with the size of the metallic spots found with MIM (Fig. 1e).

Our MIM results add evidence to the notion that unidentified physics is at work in the Kondo insulating state in  $\text{SmB}_6$ , beyond that of a simple renormalized band insulator. While the observed states seem to be consistent with topological protection at low temperatures, their robustness at high temperatures calls for new principles. This opens up the possibility of unconventional finite temperature topological protection, which has been discussed within the context of deconfinement phases in theories controlled by discrete gauge symmetry, such as the toric code in four or more dimensions<sup>42</sup>. Since a stable finite temperature topological order would be robust against thermal decoherence,

these one-dimensional channels may have profound applications in topological quantum computing if unconventional topological protection can be shown.

## **Methods**

### *Crystal characterization and surface preparation*

Prior to measurement, the resistivity of the  $\text{SmB}_6$  crystals is measured using a Quantum Design Physical Property Measurement System (PPMS). The crystal surface is prepared for MIM measurements by cleaving using a ceramic top post. The post is glued to the top surface using Loctite Hysol EA 1C epoxy (torr seal) and cured at  $60^\circ\text{C}$  for at least 2 hours. The crystal cleaves along the (001) axis, exposing a flat surface with a few step edges. Cleaving is used instead of polishing to preserve the intrinsic step edges on the exposed surface. The cleaved sample is mounted on a chip holder and grounded with wire bonding or silver epoxy before loading on piezo scanning modules in the MIM cryostat.

### *Scanning MIM measurements*

The MIM tips are batch fabricated shield cantilevers from PrimeNano Inc. using methods described in Ref. 26. The tips are mounted on a custom-made holder with an impedance-matched microwave line. The reflected MIM signal is amplified with a cryogenic microwave amplifier close to the tip. Approach to the sample is performed by monitoring the MIM signal. The scanning measurements are performed at a resonance near 1 GHz, determined by sweeping the input frequency and monitoring the total reflected power.

### *COMSOL Simulations*

Electric simulations are performed with the AC/DC module in COMSOL. Realistic parameters for the sample permittivity and sample resistivity are used:  $\epsilon \sim 600$  [43] and  $\rho \sim 30 \text{ Ohm}\cdot\text{cm}$  [25]. To qualitatively capture the tip impedance during scanning, a 2-dimensional axisymmetric model is used to approximate the 3-dimensional structure in  $\text{SmB}_6$ . A 10-nm-wide (20 nm diameter after radial symmetrization) vertical metallic strip is used to simulate the conducting wire. For the comparison to the non-contact scan, a  $\text{WTe}_2$  scan was referenced instead of non-contact scans over  $\text{SmB}_6$ . This is because the  $\text{SmB}_6$  conducting channels resides on top of step edges, and the background topographic

MIM signal prevents identification of the conducting channels in non-contact scans. In  $\text{WTe}_2$ , the exfoliated 2-dimensional sheets are very flat and there is almost no background topographic signal. While the geometry of the  $\text{WTe}_2$  conducting channel is not the same as that in  $\text{SmB}_6$ , the qualitative difference between ohmic contact and non-contact signal differences are still valid.

For the electric potential distribution simulations, the metallic tip is first set at 1 V and the bottom of the sample slab set at ground. Then the equilibrium potential is calculated using finite element analysis. For the tip-defect separation dependence simulations, the position of the tip is fixed and the lateral position of the defect is swept to mimic the scanning process.

### **Data availability**

The data used to generate the images and plots in this work are available from the corresponding author upon request.

### **Acknowledgements**

We thank Y. S. Eo, S. Saha, J. Paglione, S. Sebastian, L. Taillefer, Y. He, S. D. Chen, S. Sinha, C. Kurdak, R. J. Slager, D.-H. Lee, S. Kivelson, and T. P. Devereaux for useful discussions. The work at Stanford is supported by the Gordon and Betty Moore foundation through the Emergent Phenomena in Quantum Systems (EPiQS) initiative GBMF4546 to Z.-X.S., and DOE Office of Science, Division of Materials Science and Engineering. Work at the University of Warwick is supported by EPSRC, UK through Grant EP/T005963/1. M. B. is supported by the Marvin Chodorow postdoctoral fellowship.

### **Author contributions**

K.-J.X., J.Z., and Z.-X.S. designed the experiments. K.-J.X. performed the measurements. K.-J.X. and M.E.B. performed data analysis and simulations. E.Y.M. implemented instrumentation. J.X., M.C.H., and G.B. grew and characterized the samples. K.-J.X., M.E.B. and Z.-X.S. wrote the paper with inputs from all authors.

### **Competing interests**

Z.-X.S. is a cofounder of PrimeNano Inc., which licensed the scanning MIM technology from Stanford University for commercial instruments. This work was performed on a custom low-temperature scanning MIM instrument independent from PrimeNano Inc., except the shielded MIM tips which were purchased from PrimeNano Inc.

## References

- <sup>1</sup> Menth, A., Buehler, E. & Geballe, T. Magnetic and semiconducting properties of SmB<sub>6</sub>. *Phys. Rev. Lett.* **22**, 295 (1969).
- <sup>2</sup> Dzero, M., Xia, J., Galitski, V., & Coleman, P. Topological Kondo insulators. *Annu. Rev. Condens. Matter Phys.* **7**, 249 (2016).
- <sup>3</sup> Checkelsky, J. G. et al. Quantum interference in macroscopic crystals of nonmetallic Bi<sub>2</sub>Se<sub>3</sub>. *Phys. Rev. Lett.* **103**, 246601 (2009).
- <sup>4</sup> Eo, Y.S. et al. Transport gap in SmB<sub>6</sub> protected against disorder. *Proc. Natl. Acad. Sci.* **116**, 12638 (2019).
- <sup>5</sup> Coleman, P. Heavy fermions and the Kondo lattice: a 21<sup>st</sup> century perspective. arXiv:1509.05769 (2015).
- <sup>6</sup> Li, L., Sun, K., Kurdak, C. & Allen, J. W. Emergent mystery in the Kondo insulator samarium hexaboride. *Nat. Rev. Phys.* **2**, 463 (2020).
- <sup>7</sup> Wolgast, S. et al. Low-temperature surface conduction in the Kondo insulator SmB<sub>6</sub>. *Phys. Rev. B* **88**, 180405(R) (2013).
- <sup>8</sup> Kim, D. et al. Surface Hall effect and nonlocal transport in SmB<sub>6</sub>: evidence for surface conduction. *Sci. Rep.* **3**, 3150 (2013).
- <sup>9</sup> Kim, D., Xia, J. & Z. Fisk. Topological surface state in the Kondo insulator samarium hexaboride. *Nat. Mater.* **13**, 466 (2014).
- <sup>10</sup> Syers, P., Kim, D., Fuhrer, M. & Paglione, J. Tuning bulk and surface conduction in the proposed topological Kondo insulator SmB<sub>6</sub>. *Phys. Rev. Lett.* **114**, 096601 (2015).
- <sup>11</sup> Slager, R.-J., Mesaros, A., Juricic, V. & Zaanen, J. The space group classification of topological band insulators. *Nat. Phys.* **9**, 98 (2013).
- <sup>12</sup> Ran, Y., Zhang, Y. & Vishwanath, A. One-dimensional topologically protected modes in topological insulators with lattice dislocations. *Nat. Phys.* **5**, 298 (2009).
- <sup>13</sup> Slager, R.-J., Mesaros, A., Juriciv, V. & Zaanen, J. Interplay between electronic topology and crystal symmetry: Dislocation-line modes in topological band insulators. *Phys. Rev. B* **90**, 241403(R) (2014).
- <sup>14</sup> Xu, N. et al. Surface and bulk electronic structure of the strongly correlated system SmB<sub>6</sub> and implications for a topological Kondo insulator. *Phys. Rev. B* **88**, 121102(R) (2013).

- <sup>15</sup> Jiang, J. et al. Observation of possible topological in-gap surface states in the Kondo insulator SmB<sub>6</sub> by photoemission. *Nat. Commun.* **4**, 3010 (2013).
- <sup>16</sup> Xu, N. et al. Direct observation of the spin texture in SmB<sub>6</sub> as evidence of the topological Kondo insulator. *Nat. Commun.* **5**, 4566 (2014).
- <sup>17</sup> Neupane, M. et al. Surface electronic structure of the topological Kondo-insulator candidate correlated electron system SmB<sub>6</sub>. *Nat. Commun.* **4**, 2991 (2013).
- <sup>18</sup> Ohtsubo, Y. et al. Non-trivial surface states of samarium hexaboride at the (111) surface. *Nat. Commun.* **10**, 2298 (2019).
- <sup>19</sup> Hlawenka, P. et al. Samarium hexaboride is a trivial surface conductor. *Nat. Commun.* **9**, 517 (2018).
- <sup>20</sup> Hamasaki, H., Tokumoto, Y. & Edagawa, K. Dislocation conduction in Bi-Sb topological insulators. *Appl. Phys. Lett.* **110**, 092105 (2017).
- <sup>21</sup> Hamasaki, H., Tokumoto, Y. & Edagawa, K. Conductive and Non-conductive Dislocations in Bi-Sb Topological Insulators. *J. Phys. Soc. Jpn.* **89**, 023703 (2020).
- <sup>22</sup> Lai, K., Kundhikanjana, W., Kelly, M. A. & Shen, Z.-X. Nanoscale microwave microscopy using shielded cantilever probes. *Appl. Nanosci.* **1**, 13 (2011).
- <sup>23</sup> Lai, K., Kundhikanjana, W., Kelly, M. A. & Shen, Z.-X. Modeling and characterization of a cantilever-based near-field scanning microwave impedance microscope. *Rev. Sci. Instrum.* **79**, 063703 (2008).
- <sup>24</sup> Ma, E. Y. et al. Mobile metallic domain walls in an all-in-all-out magnetic insulator. *Science* **350**, 538-541(2015).
- <sup>25</sup> Ciomaga Hatnean, M., Lees, M. R., Paul, D. M. & Balakrishnan, G. Large, high quality single-crystals of the new Topological Kondo Insulator, SmB<sub>6</sub>. *Sci. Rep.* **3**, 3071 (2013).
- <sup>26</sup> Yang, Y. et al. Batch-fabricated cantilever probes with electrical shielding for nanoscale dielectric and conductivity imaging. *J. Micromech. Microeng.* **22**, 115040 (2012).
- <sup>27</sup> Lai, K. et al. Imaging of Coulomb-driven quantum Hall edge states. *Phys. Rev. Lett.* **107**, 176809 (2011).
- <sup>28</sup> Cui, Y.-T. et al. Unconventional Correlation between Quantum Hall Transport Quantization and Bulk State Filling in Gated Graphene Devices. *Phys. Rev. Lett.* **117**, 186601 (2016).
- <sup>29</sup> Shi, Y. et al. Imaging quantum spin Hall edges in monolayer WTe<sub>2</sub>. *Sci. Adv.* **5**, eaat8799 (2019).

- <sup>30</sup> Akintola, K. et al. Freezing out of a low-energy bulk spin exciton in SmB<sub>6</sub>. *npj Quant. Mater.* **3**, 36 (2018).
- <sup>31</sup> Gol'dshtein, I. Y., Molchanov, S. A. & Pastur, L. A. A pure point spectrum of the stochastic one-dimensional schrödinger operator. *Funct. Anal. Appl.* **11**, 1 (1977).
- <sup>32</sup> Phelan, W. A. et al. Correlation between Bulk Thermodynamic Measurements and the Low-Temperature-Resistance Plateau in SmB<sub>6</sub>. *Phys. Rev. X* **4**, 031012 (2014).
- <sup>33</sup> Denlinger, J. D. et al. Temperature dependence of linked gap and surface state evolution in the mixed valent topological insulator SmB<sub>6</sub>. Preprint at arXiv <https://arxiv.org/abs/1312.6637> (2013).
- <sup>34</sup> Nabarro, F. R. N. *Theory of Crystal Dislocations* (Dover Publications, New York, 1987).
- <sup>35</sup> Ju, L. et al. Topological valley transport at bilayer graphene domain walls. *Nature* **520**, 650 (2015).
- <sup>36</sup> Nayak, A. K. et al. Resolving the topological classification of bismuth with topological defects. *Sci. Adv.* **5**, eaax6996 (2019).
- <sup>37</sup> Slager, R.-J., Juricic, V., Lahtinen, V. & Zaanen, J. Self-organized pseudo-graphene on grain boundaries in topological band insulators. *Phys. Rev. B* **93**, 245406 (2016).
- <sup>38</sup> Li, G. et al. Two-dimensional Fermi surface in Kondo insulator SmB<sub>6</sub>. *Science* **346**, 1208 (2014).
- <sup>39</sup> Tan, B. S. et al. Unconventional Fermi surface in an insulating state. *Science* **349**, 287 (2015).
- <sup>40</sup> Cooley, J. C., Aronson, M. C., Fisk, Z. & Canfield, P. C. SmB<sub>6</sub>: Kondo insulator or exotic metal? *Phys. Rev. Lett.* **74**, 1629 (1995).
- <sup>41</sup> Hartstein, M. et al. Fermi surface in the absence of a Fermi liquid in the Kondo insulator SmB<sub>6</sub>. *Nat. Phys.* **14**, 166 (2018).
- <sup>42</sup> Dennis, E., Kitaev, A., Landahl, A. & Preskill, J. Topological quantum memory. *J. Math. Phys.* **43**, 4453 (2002).
- <sup>43</sup> Gorshunov, B. et al. Low-energy electrodynamics of SmB<sub>6</sub>. *Phys. Rev. B* **59**, 1808 (1999).

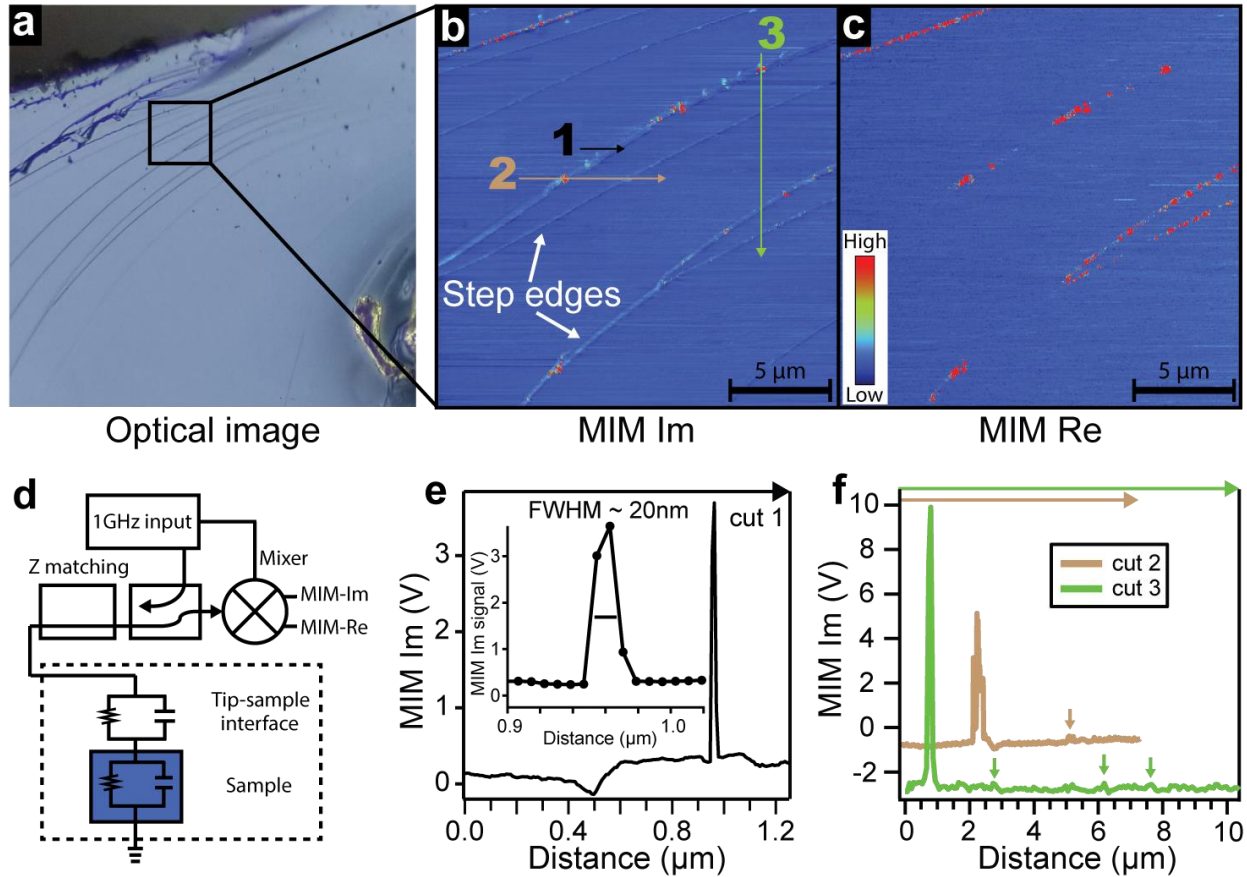


Figure 1. Scanning MIM reveals conductive spots in  $\text{SmB}_6$ . (a) Optical image of a cleaved flux-grown  $\text{SmB}_6$  surface, showing a few step edges on the surface. Bottom right area shows an aluminum inclusion, which is easily avoided during the scan. (b) MIM Imaginary (Im) channel scan of the indicated area in (a). Diagonal-running lines are topographic artifacts corresponding to the step edges, scattered red dots are ohmic contact spots. Black, brown and green lines show cuts corresponding to Fig. 1e and 1f. (c) MIM Real (Re) channel scan of the same area. (d) Image of the MIM setup and schematic of the GHz electronics. The dotted box shows the effective circuit diagram for the interface-sample system. (e) Cut corresponding to the black line in Fig. 1b. Inset is an enlarged plot showing the narrow width of the ohmic contact spot. (f) Cuts corresponding to the brown and green lines in Fig. 1b, showing the large signal at the ohmic contacts spots compared to the topographic feature signals (latter indicated by arrows). Curves are offset vertically for clarity.

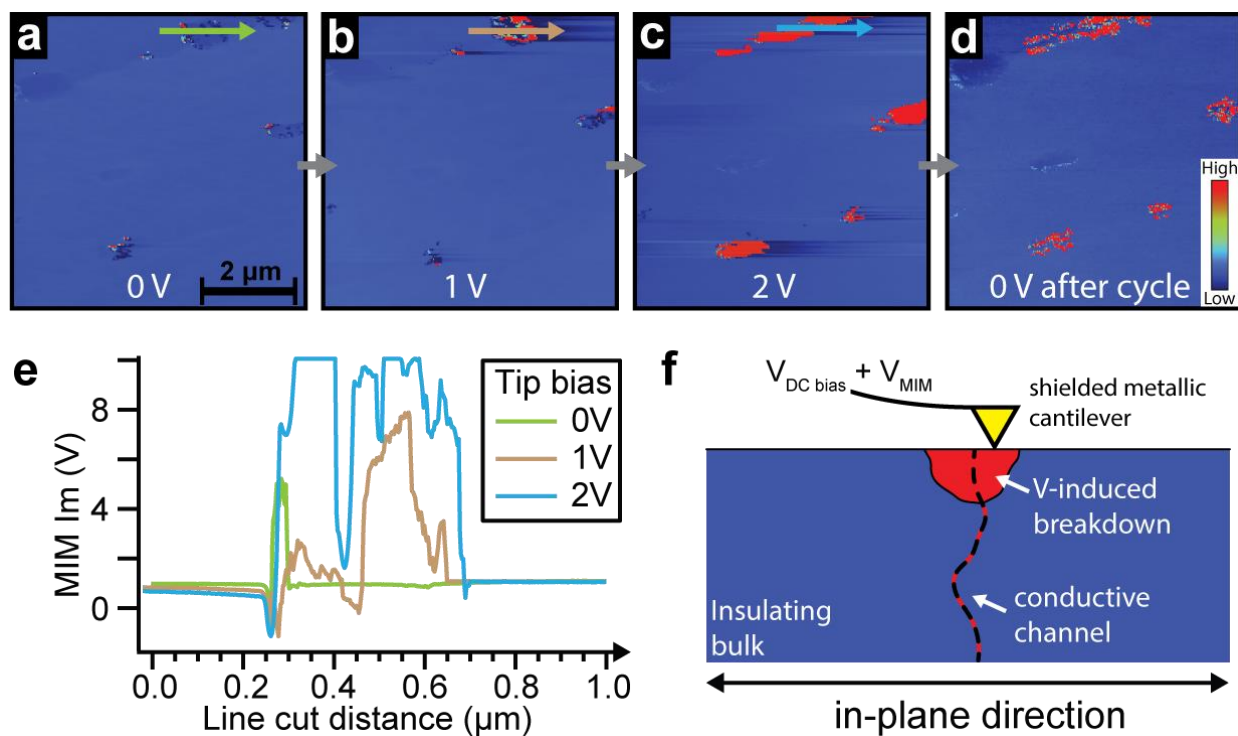


Figure 2. Bias voltage dependence and V-induced breakdown. (a)-(d) MIM-Im images of the same region, with the different tip bias indicated below each panel. Green, brown, and yellow lines near the top of panels (a)-(c) correspond to profiles shown in Fig. 2e. (e) Cuts corresponding to the colored lines in (a)-(c) and the tip bias voltages indicated in the legend. The flat top in the 2 V curve indicate saturated measurement range. (f) Cross section schematic of the voltage-induced breakdown around a conductive 1-dimensional channel within the insulating bulk of  $\text{SmB}_6$ .

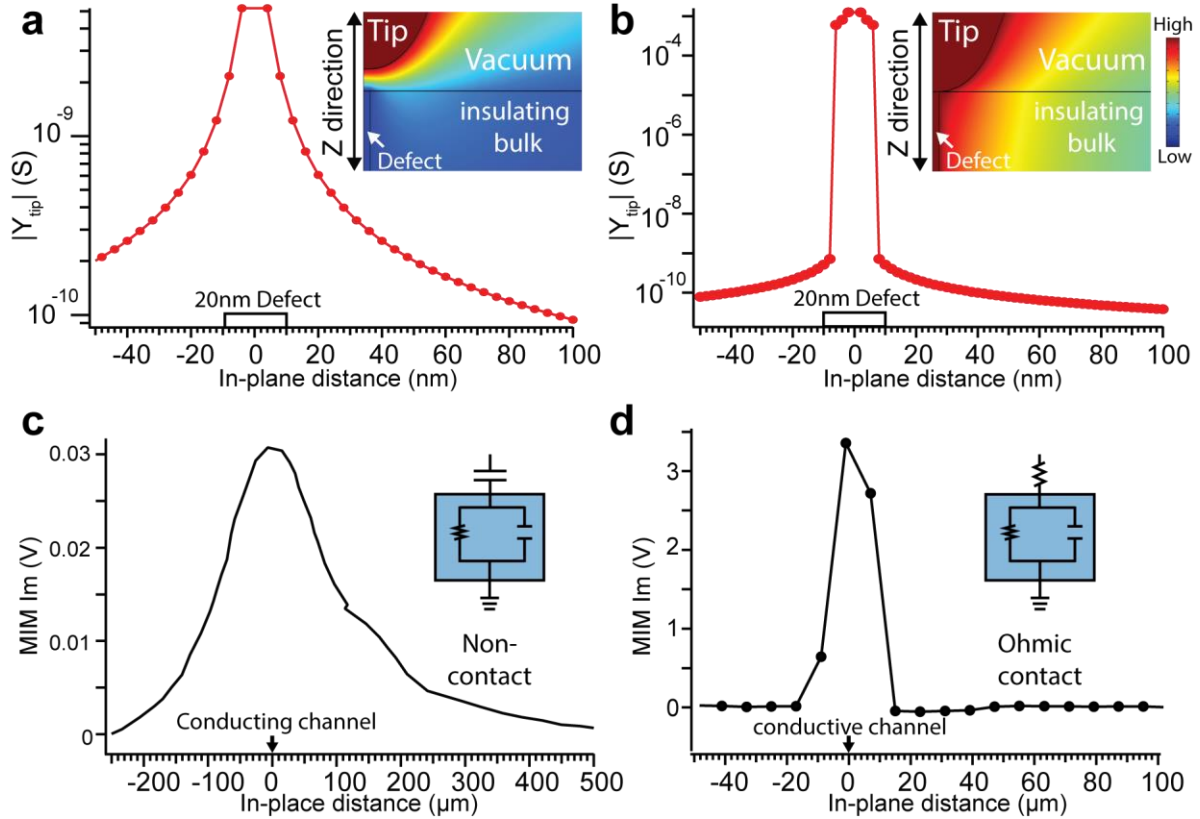


Figure 3. Qualitative comparison between simulation and experiment of the tip-defect-sample junction. (a) Simulated impedance of a non-contact line scan across a 20 nm diameter defect. (b) Simulated impedance of an ohmic contact line scan across a 20 nm diameter defect. The impedance jumps several orders of magnitude when the tip makes ohmic contact with the conducting defect. Insets in (a) and (b) show the electric potential distribution when the tip is on top of the conducting defect. Simulations are performed in a radial-symmetric geometry (c) Non-contact MIM-Im scan across an in-plane conducting channel in  $\text{WTe}_2$ , taken from Ref. 29. (d) Ohmic contact MIM-Im scan across a conductive channel in  $\text{SmB}_6$ , same as cut 1 in Fig. 1b. Inset in (c) and (d) show the effective circuit model for the tip-sample system in non-contact and contact geometries. MIM signal is roughly proportional to logarithm of the impedance (supplementary section 2). See the methods section and supplementary section 1 for detailed description of the simulations and MIM-Im line scans.

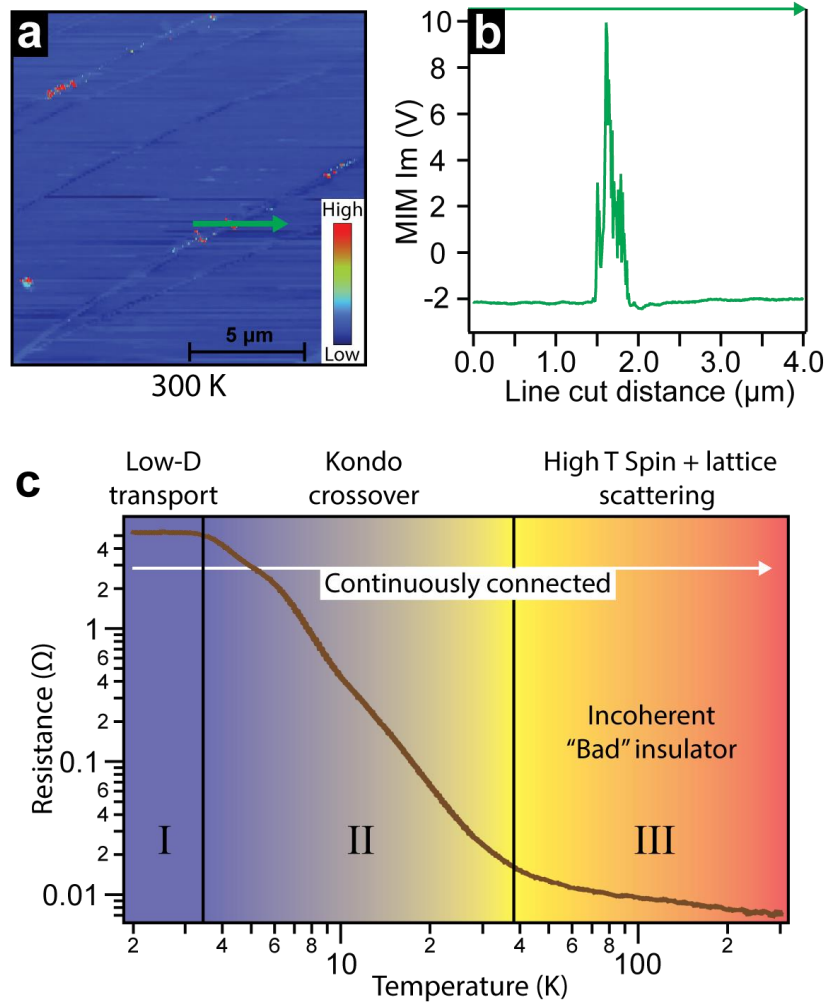


Figure 4. Temperature dependence of conductive spots. (a) MIM-Im image of  $\text{SmB}_6$  at 300 K, showing existence of conductive spots. Green line corresponds to line cut in (b), showing the MIM-Im signal at 300 K is also very large and can reach instrument saturation. (c) Resistance as a function of temperature for  $\text{SmB}_6$ , showing 3 regions: region I where transport is dominated by low-dimensional conduction; region II where Kondo coherence is established in a crossover; region III where incoherent scattering dominates at high temperatures.

*Supplementary Information for*

**Intrinsic one-dimensional conducting channels in the Kondo insulator  
SmB<sub>6</sub>**

Ke-Jun Xu<sup>1,2</sup>, Mark E. Barber<sup>1</sup>, Eric Yue Ma<sup>1,2</sup>, Jing Xia<sup>3</sup>, Monica Ciomaga Hatnean<sup>4</sup>,  
Geetha Balakrishnan<sup>4</sup>, Jan Zaanen<sup>5</sup> and Zhi-Xun Shen<sup>1,2, †</sup>

<sup>1</sup> Geballe Laboratory for Advanced Materials, Department of Physics and Applied  
Physics, Stanford University, Stanford, California 94305, USA

<sup>2</sup> Stanford Institute for Materials and Energy Sciences, SLAC National Accelerator  
Laboratory, 2575 Sand Hill Road, Menlo Park, California 94025, USA

<sup>3</sup> Department of Physics and Astronomy, University of California, Irvine, California  
92697, USA

<sup>4</sup> Department of Physics, University of Warwick, Coventry, CV4 7AL, UK

<sup>5</sup> Instituut-Lorentz for Theoretical Physics, ΔITP, Leiden University, Niels Bohrweg 2,  
Leiden 2333CA, The Netherlands

†: [zxshen@stanford.edu](mailto:zxshen@stanford.edu)

## 1. MIM signal scale and processing

The scale of the MIM signal is generally only compared qualitatively across different scans, temperature, and samples due to several reasons:

1. The MIM signal is roughly a logarithm function of the local resistivity with a sensitivity window between  $\sim 10^{-2}$  to  $\sim 10^2$   $\Omega\text{cm}$  at 1 GHz probing frequency (see figure S2), thus it is very difficult to quantitatively compare small changes in resistivity of a conducting channel.
2. The large change in MIM signal here comes from a disruption of the circuit balance due to ohmic contact with the conducting channel, so the signal is largely dependent on how well the contact is made and not so much dependent on the actual conductivity of the channel. In this way, slight differences between scans can produce different signal strengths at different spots.
3. There are many cryogenic electronic components that have temperature dependences which render comparisons across different temperature very difficult. For example, the MIM signal preamplifier is situated close the sample in the cryogenic environment to reduce noise. Changes in temperature causes the amplifier behavior to change, which we mitigate through changing the amplifier bias voltages, but this process is not precise and the signals at different temperatures cannot be compared.

In this context, the MIM signals in this work are used qualitatively to demonstrate the existence of these one-dimensional conducting channels. Other complimentary techniques, such as transport on an isolated channel, are required to quantitatively study the temperature dependence of these states.

## 2. MIM response curve

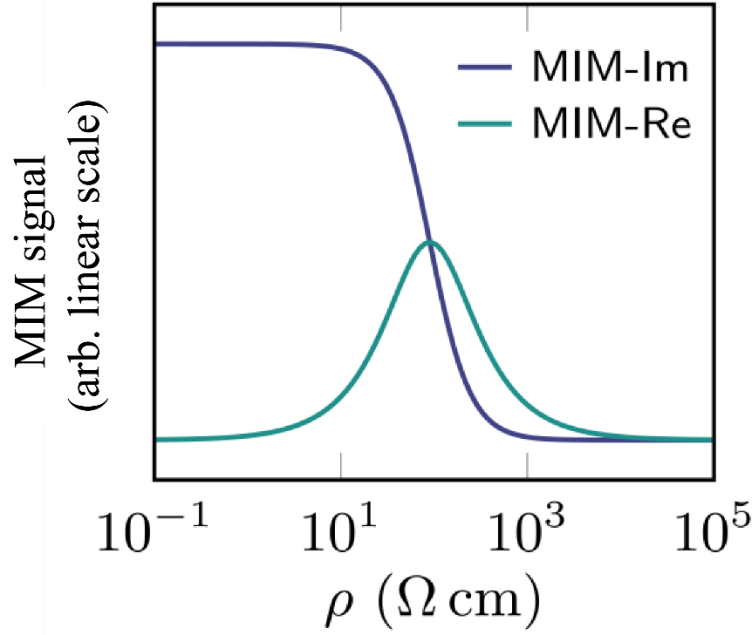


Figure S2: response curve of the MIM signal as a function of the logarithm of the resistivity. The MIM Im signal is roughly linear to the logarithm of the resistivity in the high-sensitivity window.

### 3. SmB<sub>6</sub> resistivity characterization

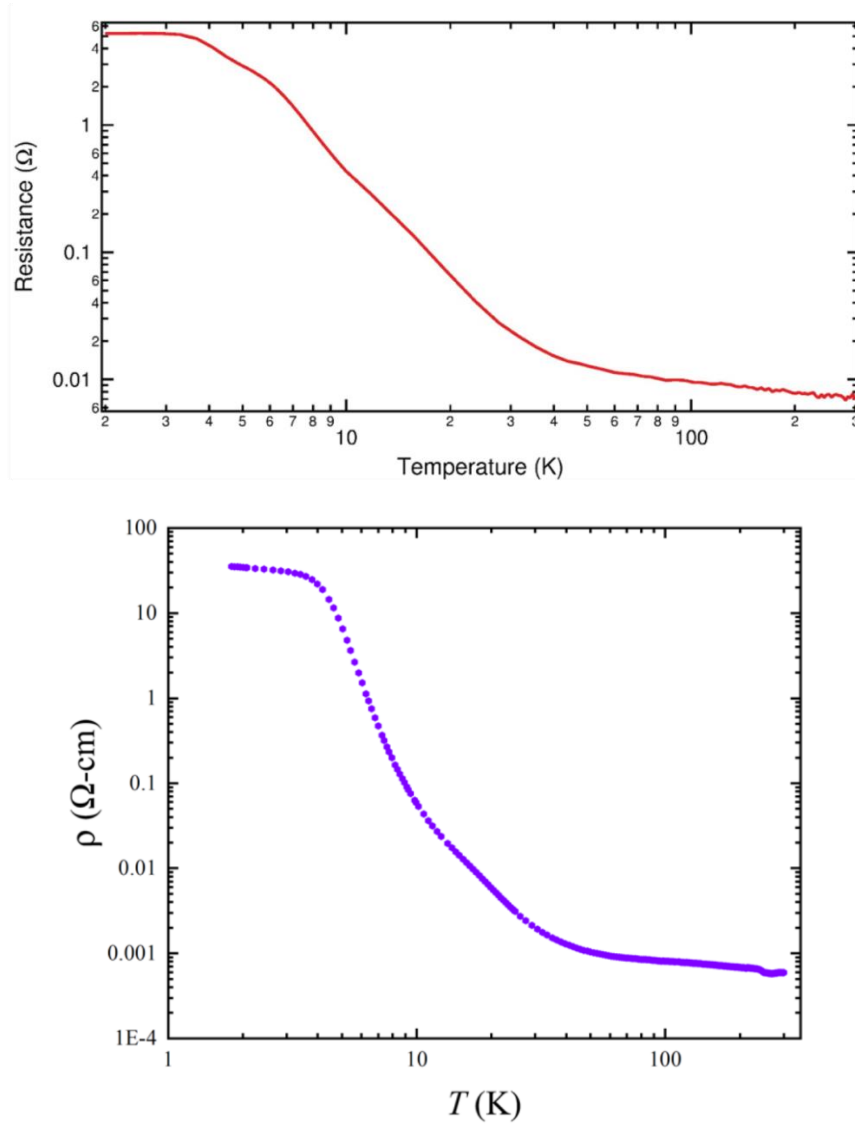


Figure S3: (top) Resistance vs. temperature for an Al-flux grown SmB<sub>6</sub> sample from the same batch as those used in the MIM studies. The flux samples were grown at UC Irvine. (bottom) Resistivity vs temperature for a floating zone grown sample used for the measurement in Supplemental section S4. The floating zone samples were grown at University of Warwick. For both types of samples, the resistivity displays activated-type insulating behavior below the Kondo coherence scale of  $\sim 40$  K. Upon further cooling, below about 5 K the resistivity saturates, previously attributed to surface state conduction.

#### 4. Repeatability of ohmic contact spots

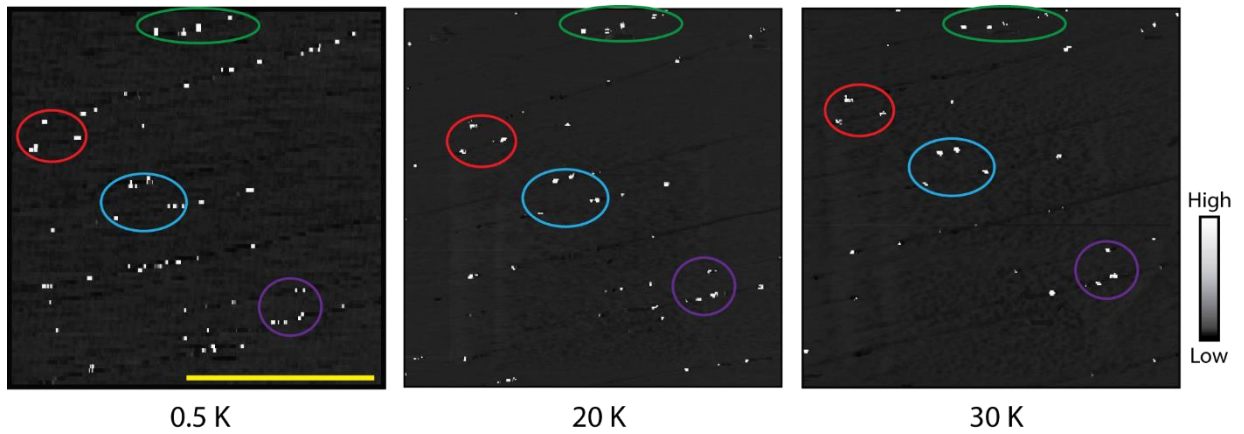


Figure S4: Repeated scans of the same area at different temperatures. The different colored circles highlight the same features in the different scans. The highly reproducible spot locations suggest that they are intrinsic to the sample, not just random ohmic contacts made to the either the bulk or surface states. Yellow scale bar is  $5\mu\text{m}$ . This is taken on the same sample as shown in Fig. 1 of the main text.

## 5. sMIM on floating zone grown $\text{SmB}_6$

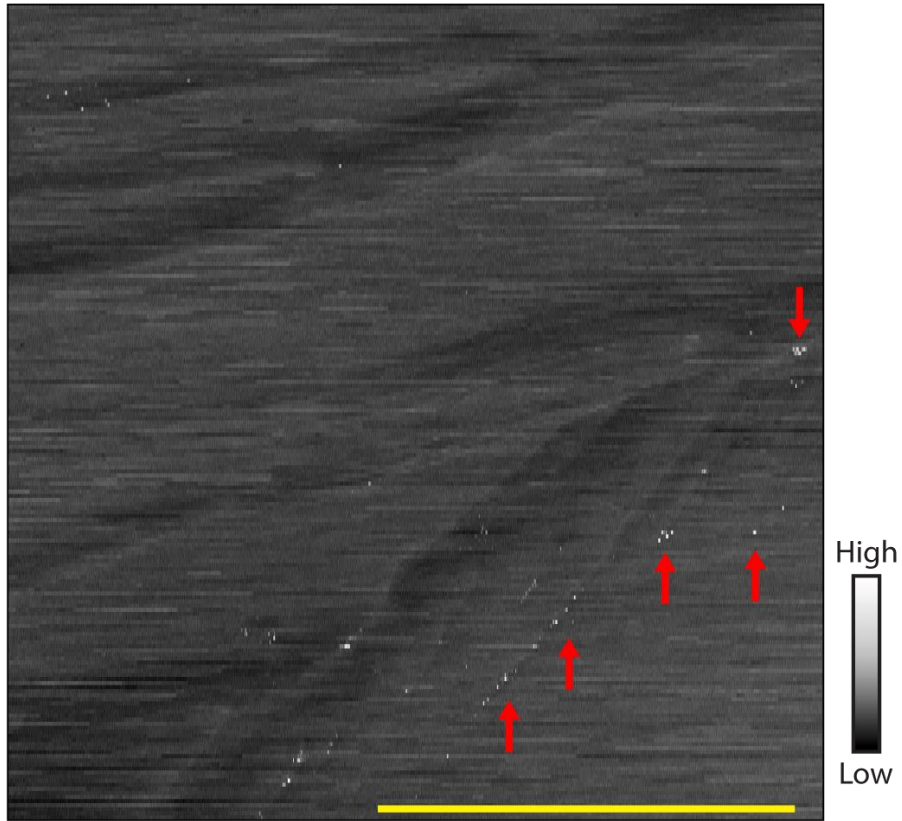


Figure S5: MIM Im image of a floating zone grown sample, taken at 77 K. Similar bright dots can be found along the step edges. Yellow scale bar is  $5\mu\text{m}$ . A few metallic spots are pointed out with red arrows.

## 6. Topography of step edges

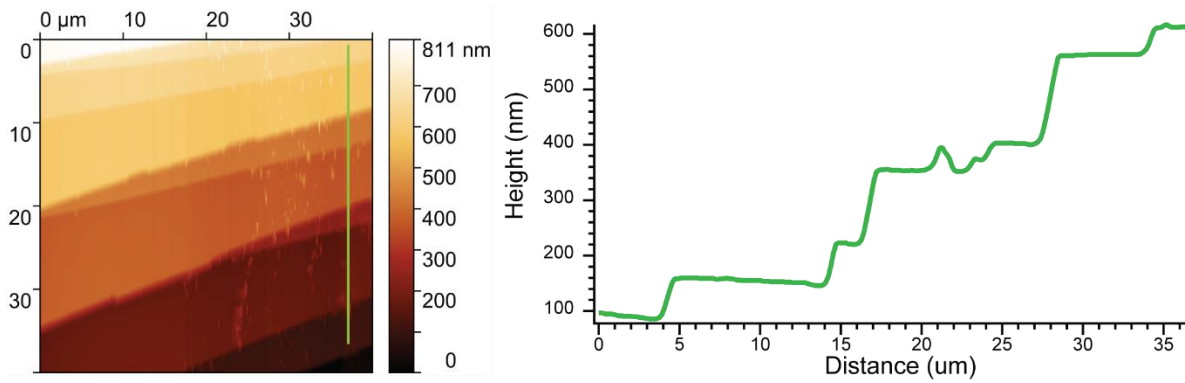


Figure S6: (left) topographic scan of the same area as in Fig. 1. (right) line cut corresponding to the vertical green line in the left panel. Each of the steps has a height of about 50 nm – 100 nm.